Available online at www.sciencedirect.com
SCIENCE DIRECT®
International Journal of Heat and Mass Transfer 48 (2005) 2722–2734
International Journal of HEAT and MASS TRANSFER
www.elsevier.com/locate/ijhmt

Heat and mass transfer predictions of the early contact of a liquid metal on an intensely cooled moving substrate

A.G. Gerber *

Department of Mechanical Engineering, University of New Brunswick, P.O. Box 4400, Fredericton, NB, Canada E3B-5A3

Received 3 May 2004; received in revised form 17 January 2005
Available online 1 April 2005

Abstract

This article describes a CFD model to predict the heat and mass transfer in the region of the initial contact of a liquid metal supplied to a cooled moving substrate. The situation resembles closely the early conditions for solid phase surface formation in many continuous casting operations. For near-net-shape applications where surface finish is important, the article describes a modeling approach for incorporating the key elements of water side cooling, intervening moving substrate, active contact layer, and liquid metal with binary-alloy solidification behavior. These elements provide the necessary macroscale results for incorporating models of the microstructure development of the cast along the surface. For the present article the results are compared to experimental data derived from the continuous casting of Al–4.5 wt%Cu.

Keywords: Near-net-shape; Melt/substrate contact; Macro-segregation; CFD model

1. Introduction

Enormous emphasis in recent years on near-net-shape casting has led to a wide variety of computational studies to support the interest in this processing paradigm. The present study also contributes to this modeling literature, but places emphasis on two features in near-net-shape casting not generally considered: (1) coupling broader influences into the prediction of the heat and mass transfer behavior in the solidification process, in particular coolant side flow and intervening substrate conditions, and (2) consideration of the interfacial contact between molten metal and substrate with surface treatment. The larger goal in emphasizing these features is an improved understanding of the conditions contributing to surface formation at or near the initial metal/substrate contact point.

The initial formation of a cast surface is considered in this study from the perspective of belt casting of Al–4.5 wt%Cu aluminum alloy sheet. A key factor in the surface forming process is surface treatment on the substrate, activated with contact of the molten metal. Understanding the heat and mass transfer behavior in response to surface treatment is important to developing improved models of observed surface microstructures. It is in this liquid/solid contact region where features, seen in the as-cast final product, are generated and subsequently "frozen" into the surface. The issue of surface quality becomes increasingly important in net-shape casting of thinner sections, which while greatly reducing the need for subsequent rolling operations, also reduces

* Tel.: +1 506 453 4513; fax: +1 506 453 5025.
E-mail address: agerber@unb.ca

0017-9310/$ - see front matter © 2005 Elsevier Ltd. All rights reserved.
doi:10.1016/j.ijheatmasstransfer.2005.01.020

Nomenclature

a	constant in Arrhenius contact model
$A(T_m)$	Arrhenius function representing contact model response
B	solid phase turbulence damping constant ($B = 100$)
c	species composition
c_p	specific heat
D	binary diffusion coefficient
E	constant in Arrhenius contact model
f	mass fraction
h	enthalpy
h_f	heat of fusion
H	cast thickness
k	thermal conductivity
k_0	permeability material constant
k_p^*	effective partition coefficient
k_p	equilibrium partition coefficient
k_μ	permeability factor
L	length of substrate in model
m_s, m_l	slope of solidus/liquidus lines
$\dot{m}$	mass flow
M_I	momentum source due to decomposition of surface stress tensor
R	universal gas constant
R_c	contact layer thermal resistance
S_g	gas phase mass source (contact zone)
S_d	mass diffusion source (contact zone)
S_h	energy source (contact zone)
$S_{\phi 1}$	volume integral source term (Table 1)
$S_{\phi 2}$	surface integral source term (Table 1)
T	temperature
T_s, T_l	solidus and liquidus temperatures
T_i	melt inlet temperature
T_m	contact zone temperature or pure metal melting temperature
T_w	substrate temperature along contact zone
T_f	melt temperature along contact zone
u_i	mixture velocity ($=f_s u_{si} + f_l u_{li}$)
u_{si}	solid phase velocity
u_{li}	liquid phase velocity
U_b	substrate (belt) velocity
V_{cv}	volume of control-volume

Greek symbols

α	volume fraction
δ	thickness of contact layer
ε	turbulent dissipation
ϕ	general scalar
κ	turbulent kinetic energy
μ	dynamic viscosity (molecular)
μ_t	turbulent viscosity
ρ	density
$\sigma_t\sigma_\kappa$ $\sigma_\varepsilon\sigma_\alpha$	turbulent Prandtl/Schmidt number
τ_{ij}	surface stress tensor
Δn_j	outward unit vector
Δt	time step
Φ	species/enthalpy slip contributions
Γ	molecular diffusion coefficient for species α
$\Gamma_\kappa\Gamma_\varepsilon\Gamma_\alpha$	turbulent diffusion coefficients

Superscripts

α	alloy component
β	base component
0	initial condition

Subscripts

e	eutectic
eff	effective transport property (molecular + turbulent)
g	gas/vapor phase
g − l	difference between gas and liquid state
ip	integration point
l	liquid phase
le	liquidus–eutectic intersection
0	initial value
s	solid phase
se	solidus–eutectic intersection

the possibility of correcting the surface defects. The present work describes a CFD model developed to predict conditions during the initial formation of a cast surface.

Much emphasis has been placed on the application of CFD methods to solidification problems using fixed grids, which include predictions of macro-segregation in the final cast [1–7]. Most of the processes considered in these studies involve flow conditions with no or relatively low forced convection, so that thermal and solutal buoyancy remain an important influence on the solidification and segregation behavior. Excellent examples of this are CFD models applied to the DC casting of aluminum [3,4] and freeze coating studies [5]. In the present case forced convection dominates the metal flow behavior in the vicinity of the contact region allowing the influence of buoyancy to be neglected. Research on macro-segregation in flows characterized by forced convection has been conducted [6,7], however none have emphasized the tightly coupled heat transfer elements that comprise the initial contact region with a view toward surface formation. The CFD model of Gerber et al. [8] has considered this coupled heat transfer problem, with an emphasis on the influence of a thermally activated "contact layer" between the molten metal

and substrate. The present study furthers this research by incorporating macro-segregation predictions into the overall solution, and examines the influence of the thermally activated contact zone on near surface solid fraction levels, temperatures and alloy compositions.

2. Governing equations

The surface conditions leading to the initial formation of the solid skin is difficult to predict due to the tight coupling of several distinct zones in the casting process. These zones each contain their own combination of physical models, and yet must be solved in a tightly coupled manner to determine the overall behavior of the cast. The basic zones are shown in Fig. 1, and include water-side cooling (zone B), a moving substrate (zone C), active contact layer (zone D), and liquid metal which can change phase (zone A). While all the zones must be solved together in the solution strategy, each zone will described separately in terms of the models employed to describe heat and/or mass transfer behavior.

To present the governing equations for each zone in a compact manner, Table 1 has been provided. A general convection–diffusion equation, with source term, is applied for each dependent variable in the solution with coefficients and source terms as outlined in the table. Details of the implementation for each zone now follow.

3. Melt zone

To account for solidification in the melt a fixed-grid binary alloy phase-change model was implemented, where the fully liquid, two-phase liquid and solid, and fully solid regions can be resolved on a single non-moving grid. The incorporation of the solidification model with species transport follows the spirit of the continuum mixture approach developed by Bennon and Incropera [9,10] with modifications related to CFD implementation in a non-segregated finite-volume/finite-element solution approach. For the melt the governing energy equation conserves the diffusion, advection, and transient evolution of sensible and latent heat in the domain, while the momentum equations account for the presence of solid and its resistance to fluid motion. Turbulence equations are modified to account for the damping of turbulence as a significant solid fraction develops. Due to the potential role of macro-segregation on final surface quality, a model for species transport is also included.

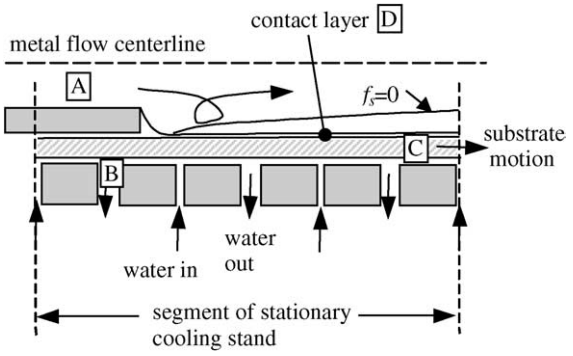

Fig. 1. Schematic of initial contact zone typical of many strip casting configurations.

The solidification model uses a continuum treatment that involves solving transport equations for the mixture enthalpy, h, and mixture mass fraction of species c^{α} (the primary alloying component). The mixture enthalpy is defined as

$$h = f_s h_s + f_l h_l \tag{1}$$

where for each phase the enthalpy is

$$\begin{aligned} h_s &= c_{ps} T \\ h_l &= c_{pl} T + (c_{ps} - c_{pl}) T_e + h_f \end{aligned} \tag{2}$$

In this treatment the specific heats of each phase, c_{ps} and c_{pl}, are assumed constant and the heat of fusion, h_f, is fixed at the eutectic temperature T_e. The solid enthalpy uses a reference of zero at $T = 0$ K. The liquidus, solidus and eutectic enthalpy boundaries must be defined in order to determine the mixture temperature; this is described fully in Appendix A. For a full description constitutive equations for mass fraction, f, and volume fraction, α, describing the solid and liquid phases, "s" and "l", in the continuum are

$$\begin{aligned} f_s + f_l &= 1 \\ \alpha_s + \alpha_l &= 1 \\ f_s &= \frac{\alpha_s \rho_s}{\rho} \\ f_l &= \frac{\alpha_l \rho_l}{\rho} \end{aligned} \tag{3}$$

while within (and across) phases the distribution of species α and β are represented as follows:

$$\begin{aligned} c^{\alpha} &= c_s^{\alpha} f_s + c_l^{\alpha} f_l \\ c^{\beta} &= c_s^{\beta} f_s + c_l^{\beta} f_l \\ c^{\alpha} + c^{\beta} &= 1 \\ c_s^{\alpha} + c_s^{\beta} &= 1 \\ c_l^{\alpha} + c_l^{\beta} &= 1 \end{aligned} \tag{4}$$

where β is taken as the base component, and a transport equation is solved for the distribution of component α in the α–β mixture. The phase diagram for the binary mixture is described in Appendix A, and Eqs. (3) and (4) can be used for computing local equilibrium states from the phase diagram. In the present analysis the temperature, T, is assumed the same between phases, and details of

Table 1
Governing equations for the melt, substrate and water zones

General convection–diffusion equation: $\frac{\partial \rho\phi}{\partial t}+\frac{\partial}{\partial x_j}(\rho u_j\phi)=\frac{\partial}{\partial x_j}\left(\Gamma_{\text{eff}}\frac{\partial\phi}{\partial x_j}\right)+S_{\phi 1}+S_{\phi 2}$

	ϕ	Γ_{eff}	$S_{\phi 1}$	$S_{\phi 2}$
Melt zone				
Mass	1	0	0	0
Momentum	u_i	$\mu+\mu_t$	$-\frac{\partial p}{\partial x}+\frac{\mu}{k_\mu}(u_{si}-u_i)+M_i$	0
Energy	h	$k/c_P+\mu_t/\sigma_t$	0	$-\frac{\partial}{\partial x_j}(\rho(h_l-h)(u_j-u_{sj}))$
Species	c^α	$\rho D+\mu_t/\sigma_\alpha$	0	$-\frac{\partial}{\partial x_j}(\rho(c_l^\alpha-c^\alpha)(u_j-u_{sj}))$ where $c_l^\alpha-c^\alpha=c_s^\alpha f_s\left(\frac{1}{k_p^*}-1\right)$
Turbulent kinetic energy	κ	$\mu+\mu_t/\sigma_k$	$P_k-\rho\varepsilon-\kappa B\frac{(1-f_l)^2}{f_l^3}$	0
Turbulent dissipation	ε	$\mu+\mu_t/\sigma_\varepsilon$	$\frac{\varepsilon}{\kappa}(c_{\varepsilon 1}P_k-\rho c_{\varepsilon 2}\varepsilon)-\varepsilon B\frac{(1-f_l)^2}{f_l^3}$	0
Substrate zone				
Energy	h	k/c_p	0	0
Note: Convective term uses specified substrate velocity (U_b).				
Water cooling zone				
Mass	1	0	0	0
Momentum	u_i	$\mu+\mu_t$	$-\frac{\partial p}{\partial x}+M_i$	0
Energy	h	$k/c_p+\mu_t/\sigma_t$	0	0
Turbulent kinetic energy	κ	μ_t/σ_k	$P_k-\rho\varepsilon$	0
Turbulent dissipation	ε	μ_t/σ_ε	$\frac{\varepsilon}{\kappa}(c_{\varepsilon 1}P_k-\rho c_{\varepsilon 2}\varepsilon)$	0

how to determine T given h, c^α and f_s is described in Appendix A. Finally the mixture properties for density, ρ, and thermal conductivity, k are evaluated as

$$\rho=\alpha_s\rho_s+\alpha_l\rho_l \tag{5}$$

$$k=\alpha_s k_s+\alpha_l k_l \tag{6}$$

and the continuum molecular diffusion coefficient for the α component is calculated as

$$\Gamma=\rho(f_s D_s^\alpha+f_l D_l^\alpha) \tag{7}$$

It should be noted that while local equilibrium according to the Lever rule applies in the simulation at the microscale, non-equilibrium behavior in temperature and species transport is allowed at the macroscale. For example, while an infinite species diffusion rate is allowed at small scales in the solid phase (according to the Lever rule), in Eq. (7) the mass diffusivity of the solid (about one thousand times less than the liquid phase) reflects that observed in actual Al–Cu systems and prohibits any significant solid-state diffusion at the macroscale. The macroscale in this case would be defined by the size of the computational grid.

The fluid flow conditions in the melt zone are governed by the conservation equations for mass and momentum as outlined in Table 1. The mass conservation uses a mixture density (Eq. (5)) and a mixture velocity field defined as $u_i=f_s u_{si}+f_l u_{li}$. It is the mixture velocity that is used for all of the advection terms in the transport equations, however using this formulation for velocity results in slip contributions to the energy and species equations, which appear as source terms in Table 1.

The complete solidification model also requires modifications to the momentum equations to account for the interphase viscous drag between the evolving solid structure and the liquid metal. As a starting point in this paper a fixed solidification structure is assumed (i.e., fixed dendritic growth from the belt surface). In this regard the second term in the melt zone momentum sources (see Table 1) represents a D'Arcy-Law momentum sink [11], with k_μ a permeability factor dependent on the morphology of the solidification front, and u_{si} the solid phase velocity.

The form of the permeability factor chosen for this model is [11]

$$k_\mu=k_0 f_l^3/(1-f_l)^2 \tag{8}$$

where k_0 is a material constant that is dependent upon the solidification behavior of the particular alloy.

In the momentum equations u_i is the mixture velocity of the two phases, which in the limit of complete solidification, approaches the solid phase velocity components

(u_{si}). The terms M_i in Table 1 represent additional contributions to the source from the linearization of the surface stress tensor, τ_{ij}, which is reduced by the assumption of a Newtonian fluid in accordance with standard practice [12].

Due to the limited experimental/theoretical work on turbulence levels adjacent to a solidification front the standard two-equation κ–ε turbulence model was employed, with only minor modification, for both the melt and cooling water zones. The form of the equations is shown in Table 1. The practical approach taken here has been to add damping terms along walls with solidification so that turbulence is gradually removed with increasing solid fraction (in Table 1 see source terms, with coefficient B, for turbulent kinetic energy and dissipation). The near wall shear stresses are reduced to zero by the imposition of a zero velocity gradient in the solid through source terms in the momentum equations (i.e., D'Arcy-Law model).

The behavior of the turbulence damping terms reflects the D'Arcy-Law permeability function k_μ in the momentum equations, with the intention that as the solidification structure develops the scale of turbulent activity should be reduced in a similar way. Standard thermal wall functions were applied along all walls except for the top surface of the substrate, which required a special treatment due to the presence of the contact layer (to be described subsequently). All conservation equations were influenced by the turbulence model through the adjustment of the laminar diffusion coefficients as follows:

$$\begin{aligned} \mu_{\text{eff}} &= \mu + \mu_{\text{t}} \\ k_{\text{eff}} &= k + \mu_{\text{t}}/\sigma_{\text{t}} \\ \Gamma_\kappa &= \mu + \mu_{\text{t}}/\sigma_\kappa \\ \Gamma_\varepsilon &= \mu + \mu_{\text{t}}/\sigma_\varepsilon \\ \Gamma_\alpha &= \Gamma + \mu_{\text{t}}/\sigma_\alpha \end{aligned} \tag{9a}$$

where

$$\mu_{\text{t}} = \rho c_\mu \kappa^2/\varepsilon \tag{9b}$$

A full description of the terms in the κ–ε model and standard model constants are given in Ref. [13].

4. Contact layer zone

Along the top surface of the substrate (belt) a thin 'contact' layer is introduced between the melt and the cooling substrate. In many strip-casting processes this thin layer is comprised of a chemically inert (often refractory) material, or, a mould release agent (such as graphite or silica) that is placed onto the substrate via a carrier fluid such as water. This layer is typically very thin, beginning with a thickness of ~1 μm and increasing, when thermally activated, to ~50 to 100 μm in thickness. With this in mind the shape of the contact layer is assumed not to influence the metal flow at the surface, and the contact layer fluid moves at the speed of the substrate. Other assumptions, outlined in greater detail in [8], are thermal equilibrium within a well-mixed gas–liquid mixture in the contact region, and radiant energy transport is neglected. It should be noted that the movement of the gas after activation of the contact layer is assumed to be at the substrate speed. Due to the relatively high surface tension of aluminum, the transport of bubbles through the aluminum layer is not a problem in practice.

With the above assumptions energy transport across the contact layer can be assumed as locally one-dimensional (due to the thin nature of the layer and the high surface heat flux at ~1 MW/m^2 normal to the substrate [8]), and can be described with the equation:

$$\frac{\partial}{\partial y}\left(k\frac{\partial T_{\text{m}}}{\partial y}\right) = -S_{\text{h}} \tag{10}$$

where y is taken as the coordinate normal to the surface of the substrate. In Eq. (10), k is the mixture thermal conductivity, T_{m}, the temperature in the contact layer, and S_{h} any energy source term. If the energy required for gasification of the contact material is considered small relative to the total energy transported over the contact layer then $S_{\text{h}} = 0$ [8]. The resulting equation for energy transport appears overly simplified, however, determining the level of gas generated α_{g}, and the related thickness of the contact layer δ (the thickness over which Eq. (10) must be integrated), is not straightforward.

The governing equations (at steady-state) for mass transport in the contact layer are as follows for the gas phase:

$$\frac{\partial}{\partial x}(\rho_{\text{g}} U_{\text{b}} \alpha_{\text{g}}) = S_{\text{g}} - S_{\text{d}} \tag{11}$$

and the liquid phase,

$$\frac{\partial}{\partial x}(\rho_{\text{l}} U_{\text{b}} \alpha_{\text{l}}) = -S_{\text{g}} \tag{12}$$

where the volume fractions sum to unity ($\alpha_{\text{g}} + \alpha_{\text{l}} = 1$) and the velocity of the contact layer is assumed to move at the speed of the belt, U_{b}. In Eqs. (11) and (12) the source terms S_{g} and S_{d} represent, respectively interphase mass transfer and mass diffusion (of the gas phase) into the melt or substrate.

The mass generation for the gas phase, S_{g}, is based on a Boltzmann distribution (implied in an Arrhenius thermal activation model indicated by function $A(T_{\text{m}})$) of the fraction of molecules with energy available for gasification. This fraction is always applied to the remaining liquid along the cooling substrate as follows:

$$S_{\text{g}} = (1 - \alpha_{\text{g}})\frac{\rho_{\text{l}}}{\rho}\dot{m}_0 A(T_{\text{m}}) \tag{13}$$

where for various types of contact layers, under controlled experiments, the behavior of the function $A(T_m)$ can be determined. Assuming an Arrhenius equation to represent the activation behavior of the form $A(T_m) = ae^{-E/RT}$, the constants for the present case were $a = 1 \times 10^8$ (proportionality constant) and $E = 43{,}000$ (kJ/kmol) with R the universal gas constant (kJ/kmol K). The units for $A(T_m)$ are fraction of molecules activated per unit volume of mixture and the activating temperature (T_m) that of the contact layer. The initial mass flow of the applied contact layer is indicated by $\dot{m}_0$. The diffusion term, S_d, is intended to account for mass that diffuses into the melt, though little information is available for this. For the present investigation S_d will be assumed to be zero, although clearly this could be modified to account for high solubility gases from the dissociation of the contact layer.

While Eqs. (11) and (12) account for the movement and generation of the second phase, the total insulating effect of the contact layer, obtained by adding Eqs. (11) and (12), is governed by the equation:

$$\frac{\partial}{\partial x}(\rho U_b) = -S_d \tag{14}$$

With Eqs. (11) and (14) two equations are available for obtaining the unknowns α_g and δ, however δ does not appear explicitly in these equations. To bring δ into the equations, a finite-volume integration of Eqs. (11) and (14) is performed over a control-volume located in the contact layer as shown in Fig. 2. Assuming an arbitrary control-volume height δ, the integration of Eq. (11):

$$\oint_s (\rho_g U_b \alpha_g)\,dA = \oint_V (S_g - S_d)\,dV \tag{15}$$

with an assumed depth of unity so that $dA = \delta$ and $dV = \delta\,dx$, results in the discrete equation:

$$(\rho_g U_b \alpha_g \delta)_e - (\rho_g U_b \alpha_g \delta)_w = (S_g - S_d)\Delta x \bar{\delta} \tag{16}$$

where the East–West notation is common with finite-volume discretization techniques. Similarly for Eq. (14):

$$\oint_s (\rho U_b)\,dA = \oint_s ((\rho_{g-l}\alpha_g + \rho_l)U_b)\,dA = \oint_V (-S_d)\,dV \tag{17}$$

we arrive at the discrete equation:

$$((\rho_{g-l}\alpha_g + \rho_l)U_b\delta)_e - ((\rho_{g-l}\alpha_g + \rho_l)U_b\delta)_w = (S_g - S_d)\Delta x \bar{\delta} \tag{18}$$

Eqs. (16) and (18) provide two discrete equations for α_g and δ. The solution of this coupled non-linear equation (described in Appendix B) will provide the distribution

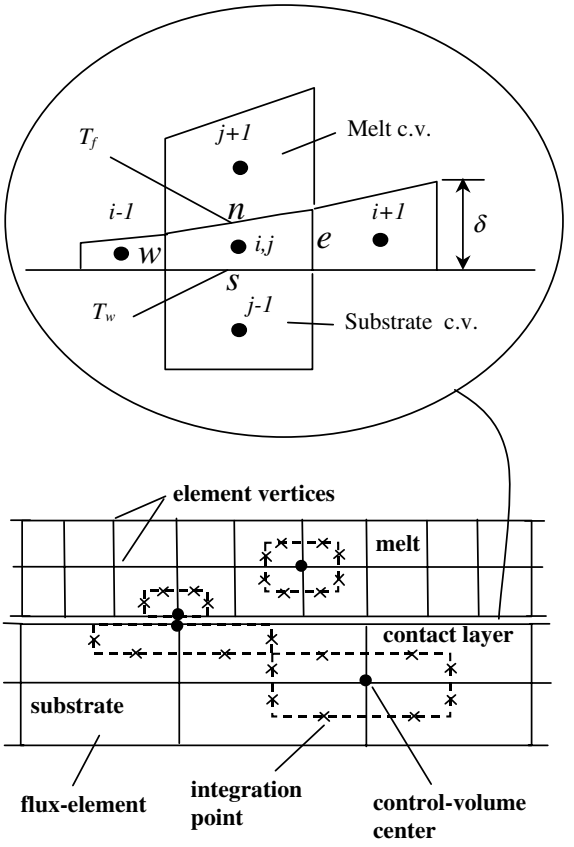

Fig. 2. Schematic of contact layer between melt and substrate and representative grid arrangement for all three zones.

for α_g and δ along the substrate length. The solution uses the latest available estimate for the contact layer temperature distribution.

With the distribution of α_g and δ determined, and since Eq. (10) implies that heat transfer through the contact layer is primarily one-dimensional, a local contact resistance, R_c, can be calculated as follows (assuming the gas separates from the heavier liquid):

$$R_c = \delta\left(\frac{\alpha_g}{k_g} + \frac{(1-\alpha_g)}{k_l}\right) \tag{19}$$

This resistance is applied when performing the finite-volume integration over control-volumes for the fluid and solid adjacent to the evolving gas layer as shown in Fig. 2. In that integration process it is assumed that the thickness δ is much smaller than the grid resolution for the CFD mesh near the surface. The contact layer temperature, T_m, used to evaluate the properties for the contact layer, can be deduced from a finite-volume integration of Eq. (10) to be simply:

$$T_m = \frac{1}{2}T_f + \frac{1}{2}T_w \tag{20}$$

5. Contact layer response

In Fig. 3a is shown a typical CFD solution (using $L = 55$ mm $H = 10$ mm and a casting speed of 0.14 m/s) including Eqs. (16), (18) and (19) to model the contact zone response. The contact layer liquid mass fraction f_l is seen to decline slightly as only a relatively small amount is (typically) consumed. However, the volume fraction of the gas phase increases rapidly, so that the resulting contact layer thickness, δ, provides a large thermal barrier to subsequent heat removal (as is apparent in the thermal resistance implied by Eq. (19)). In solving for the contact layer gas volume fraction and thickness, the latest interface temperature calculated using Eq. (20) was used. This implies an initial guess at the start of a solution, however the error is continually reduced with iteration until at steady-state the final interface temperature is obtained. In Fig. 3b is shown the final temperature distribution along the interface for the melt, contact layer and substrate surface.

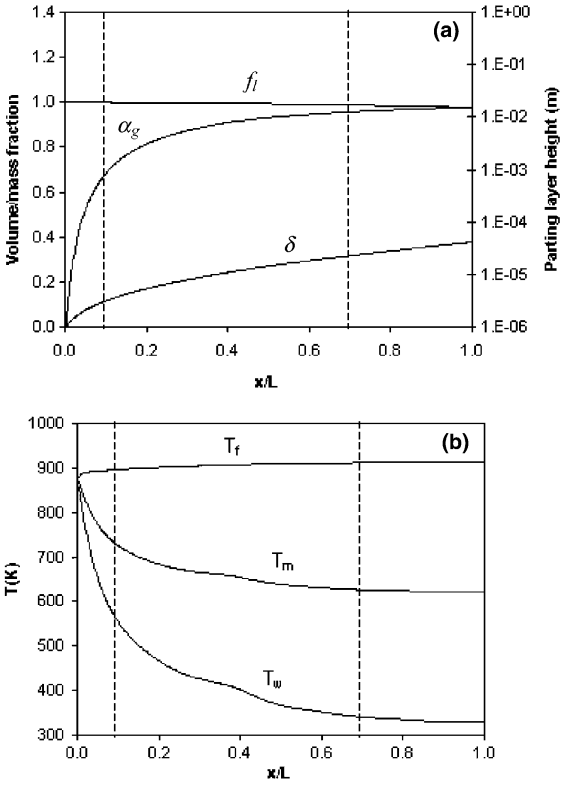

Fig. 3. Contact layer response for the case of $T_i = 988$ K, $U_b = 0.14$ m/s, $H = 10$ mm and $a = 1 \times 10^8$ where in (a) parting layer thickness (δ), vapor volume fraction (α), and contact liquid mass fraction (f_l) are shown, and in (b) melt (T_f), contact layer (T_m) and substrate wall temperature (T_w) are shown along the length of the substrate.

6. Cooling water zone

The cooling water zone operates at much higher speeds, higher pressure, and lower temperature than the melt zone. Phase change does not occur in this zone so the governing energy equation, as described in Table 1, does not include latent heat and no longer applies to a mixture of two-phases as in the melt zone, but to a single-phase fluid. In addition the mass/momentum equations are for a single-phase fluid and require no interphase drag term. The terms M_i are treated as described in the Melt zone.

Since the water is assumed incompressible the transient term in the mass conservation equation is dropped. The flow in the water zone is turbulent and requires a turbulence model as previously described for the melt zone. The form of the governing equations for turbulence is the same as employed in the melt zone except the additional damping terms associated with the appearance of the second phase are dropped.

7. Substrate zone

The substrate has a prescribed motion, defined by the casting speed of the process. Since only the speed is known a conservation equation for energy is required that includes both the advection and diffusion of energy. The energy equation for the substrate is shown in Table 1, where U_b is the prescribed velocity of the substrate (belt).

8. Numerical model: melt, substrate and cooling water zones

The model has been implemented within the general-purpose CFD software CFX-TASCflow. The CFD algorithms for this software are based on a finite-volume/finite-element discretization [14] of the conservation equations (in the present model mass, momentum, energy, species and turbulence). The discretization is nominally second order accurate, solution times are accelerated through the use of a linear multi-grid solver and a coupled solution of the momentum and mass equations [15].

The liquid and solid phase conservation equations are discretized using a conservative finite-volume integration over a control-volume. The discretization of the conservation equations, in the context of a finite-element representation of the geometry, is as follows for a general scalar ϕ,

$$\rho V_{cv}\left(\frac{\phi-\phi_0}{\Delta t}\right)+\sum_{ip}\dot{m}_{ip}\phi_{ip} = \sum_{ip}\left(\Gamma_\phi\frac{\partial\phi}{\partial x_j}\Delta n_j\right)_{ip}+S_{\phi 1}V_{cv}+S_{\phi 2} \quad (21a)$$

where

$$\dot{m}_{\mathrm{ip}} = (\rho u_j \Delta n_j)_{\mathrm{ip},0} \tag{21b}$$

and

$$S_{\phi 2} = \sum_{\mathrm{ip}} (\dot{m}_{\mathrm{ip}} - \dot{m}_{\mathrm{ip,s}}) \Phi_{\mathrm{ip}} \tag{21c}$$

In Eqs. (21) V_{cv} is the volume of the control volume, the subscript "ip" denotes an integration point, the summations indicated are over all the integration points defining a surface, Δn_j is the outward unit vector of discrete surface segment, Δt is the time step, and the subscript "0" indicates property evaluation at the old time level. In Fig. 2 is shown the location of the integration points relative to the flux-element and control-volume faces. The term $S_{\phi 1}$ represents volume integrated source terms, while $S_{\phi 2}$ represents surface integrated source terms. Referring to Table 1 and the $S_{\phi 2}$ column, Φ_{ip} would apply for the melt species equation to $(c_{\mathrm{l}}^{\alpha} - c^{\alpha})$ and for the melt energy equation to $(h_{\mathrm{l}} - h)$. In Eq. (21c) $m_{\mathrm{ip,s}}$ represents the solid mass flow (evaluated using the mixture density) at an integration point.

The basic equations, and their linearization, are further described elsewhere [16] while extensions specific to the present model were the incorporation of the solidification model with species transport, multi-zone implementation and contact layer model. Calculations were conducted to obtain grid independent solutions in terms of the solidification front profile and melt/substrate interface conditions. The total grid size was 55,700 nodes (in a 2D plane), with nodes distributed between the melt (51,100 nodes), substrate (1880) and water zones (2720). The grid was highly refined in the melt region (by grid embedding) adjacent to the substrate to capture the thermal gradients, flow recirculation, and segregation profile development.

9. Model results and discussion

In strip-casting the formation of a high quality as-cast surface under a variety of casting conditions (speeds, thickness, etc.) requires an active thermal

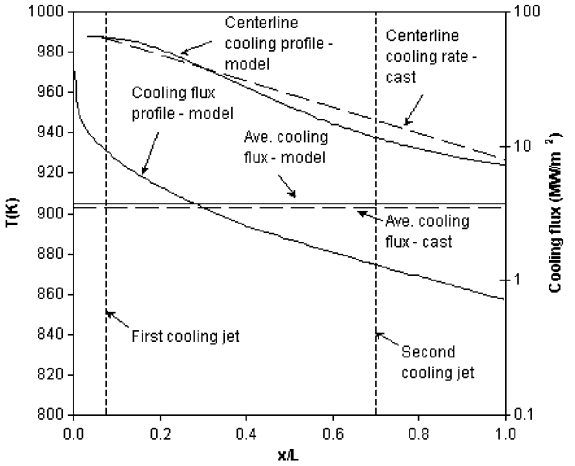

Fig. 4. Comparison of predicted surface conditions to measured casting data for Al–Cu4.5 wt% [17,18] where $T_{\mathrm{i}} = 988$ K, $U_{\mathrm{b}} = 0.14$ m/s, $H = 10$ mm and $a = 1 \times 10^8$.

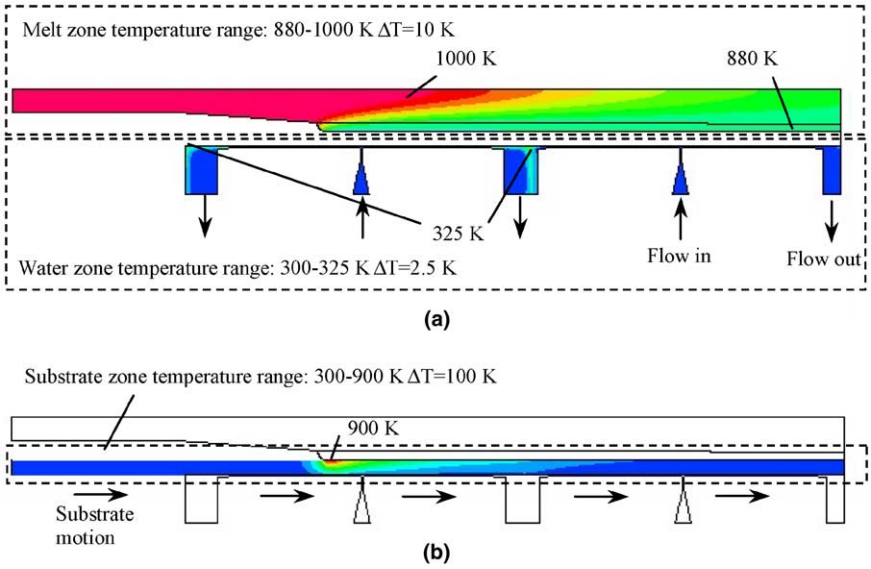

Fig. 5. Predicted conditions for Al–Cu4.5 wt% with $T_{\mathrm{i}} = 988$ K, $U_{\mathrm{b}} = 0.14$ m/s, $H = 10$ mm, $L = 55$ mm and $a = 1 \times 10^8$. Shown in part (a) temperatures in the melt and cooling water zones, and in part (b) temperature in the substrate zone.

barrier to reduce the thru-thickness thermal stress sufficiently to prevent plastic deformation. This barrier also controls cooling conditions for the metal along the moving substrate. For the present paper, a thin gas layer originating from an organic liquid (contact layer) applied to the moving substrate provides this barrier. To validate the numerical model experimental cooling data from a small-scale twin-belt caster was used. Since the CFD model accurately represents the geometry (assuming symmetry), cooling water flow rates, and casting conditions of the entrance region of this experimental system [17,18], portions of the experimental heat flux and centerline temperature profile can be used to evaluate the model accuracy.

The experimental system consists of two endless belts, one on top of the other, rotating in opposite directions. Molten aluminum metal is poured into the cavity between the two belts. Interlocking steel blocks form the edges of the mold cavity. A carefully designed injector is inserted between the belts to deliver the metal to the substrate. The belts are supported at the mold entrance, and along its length, by liquid bearings consisting of hexagonal jet nozzles arranged in a honeycomb pattern. A thin water film is maintained by this nozzle arrangement to provide the bearing surface and high heat transfer rates. A constant monitoring of the heat flux profile occurs along the belt length, and an active contact layer, a subject of this paper, can be used to modulate the heat flux level. Since the cast is wide relative to its thickness two-dimensional flow and heat transfer conditions can be assumed at the half-width location. Furthermore the belt/cooling system is identical both along the top and bottom of the cast allowing only half of the cast cross-section to be modeled.

The numerical model results were compared against heat flux and centerline temperature profile data obtained experimentally at a cast speed and thickness of $U_b = 0.14$ m/s and $H = 10$ mm, respectively. The predicted results for these casting conditions are shown in Fig. 4 where the extent of the substrate (L) considered in the simulations was 55 mm. The centerline cooling profile and the average cooling flux along the substrate are both well predicted. From this Figure important features of the casting process are apparent. At initial contact a very high cooling flux is achieved of $\sim$30 MW/m^2, and it is at this point the thermal barrier is activated. Rapid growth of the thermal barrier leads to a large reduction in the cooling flux by the time the first water cooling zone is reached. Following this the cooling flux is gradually reduced as the gas layer grows. The response of the gas layer thickness and contact layer temperatures for this case have already been described in conjunction with Fig. 3 in a previous section.

In Fig. 5 are shown the temperature distributions in the melt and water zones, as well as the belt temperature. In Fig. 6 are shown close-ups of the conditions immediately following the contact point. Rapid formation of solid and subsequent remelting occur in this region. The formation of a solid structure in the presence of strong fluid recirculation (see Fig. 6c), resulting from flow separation off the nose-tip, results in high levels of macro-segregation just following the contact point as shown in Fig. 6b. Fluid motion counter to the substrate motion onto which the forming solid is attached, results in significant interphase slip and the accumulation of c^{α} in the liquid phase. This aspect of the casting process is modeled assuming dendritic solidification, with the solid phase attaching immediately to the moving melt. If a portion of the solid structure were assumed to be detached from the substrate, either as equiaxed crystals or sheared dendrites from a columnar structure, the tendency for macro-segregation would be reduced since the interphase slip would be significantly less over a range of solid fraction. Obviously many modeling

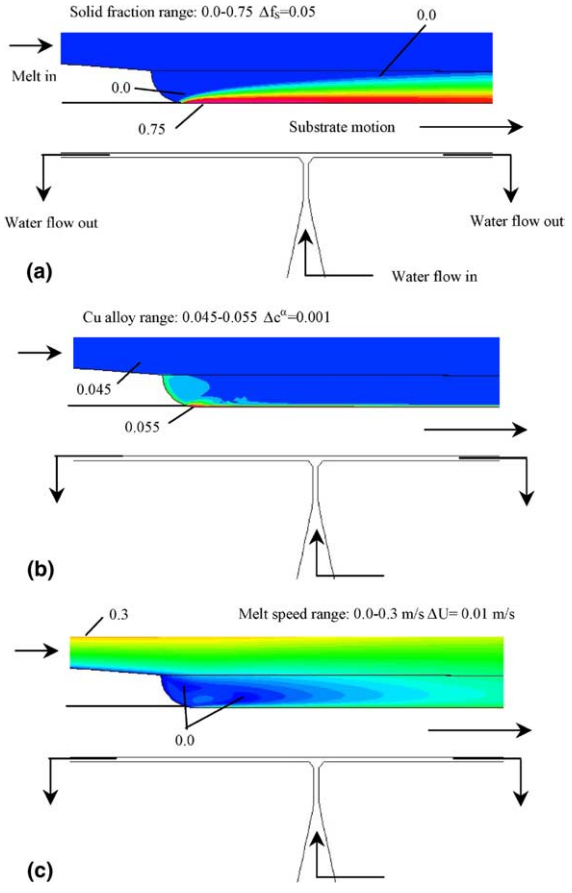

Fig. 6. Close-up view of predicted conditions for Al–Cu4.5 wt% at conditions $T_i = 988$ K, $U_b = 0.14$ m/s, $H = 10$ mm, $L = 55$ mm and $a = 1 \times 10^8$ in the region of the melt/substrate contact. Shown are profiles of (a) solid fraction, (b) composition and (c) liquid metal speed.

approaches could be taken here to represent the behavior of the solid phase development. In this paper a straightforward assumption has been taken to highlight the tendency for macro-segregation in the contact region. Due to the extremely high cooling rates near the metal contact point an effective partition coefficient of $k_p^* = 5k_p$ was employed to reflect likely reduced partitioning behavior at high solid growth rates [19]. Future studies will explore these features in more detail.

While the contact zone may have a significant build up of solute in the liquid phase, the presence of the contact layer slows the subsequent solidification allowing time for the accumulated solute to diffuse back towards its initial composition. In Fig. 7a is shown the importance of an active contact layer along the substrate length. For the most active case, $a = 1 \times 10^8$, the solid fraction level along the surface is reduced and allows, via diffusion and possibly some fluid turbulent mixing, for the c^α level to return quite rapidly to its initial composition. This is not the case when $a = 1 \times 10^7$ where large variations in c^α are frozen into the solid structure which develops rapidly as shown in Fig. 7b. The variation of c^α across the cast thickness in the contact region is carried forward along the substrate as seen in Fig. 8 where the composition and solid fraction profiles are shown at location $x/L = 1$. Here also it is apparent that with a weak contact layer the macro-segregation distribution is much more significant, since with the high solid fraction levels diffusion of the solute to its initial composition is significantly reduced. The composition and solid

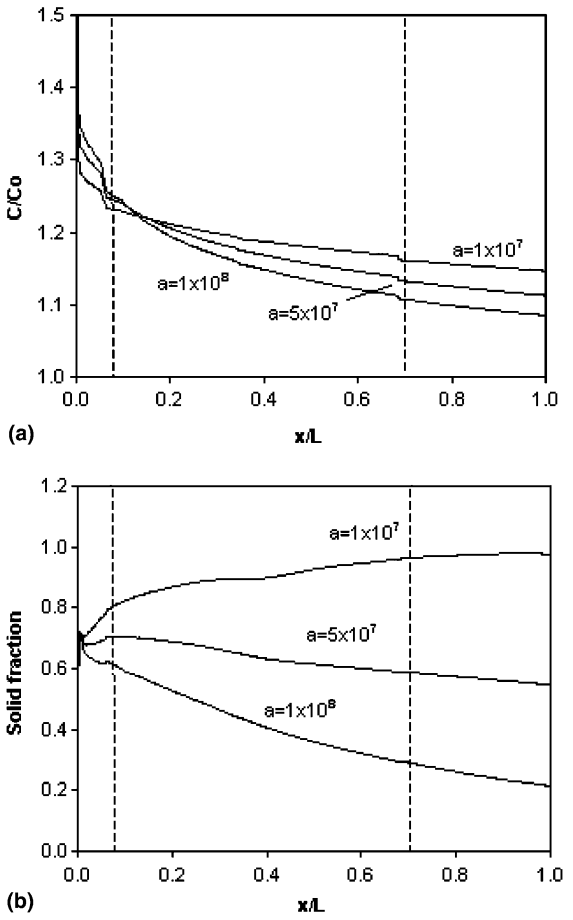

Fig. 7. Profiles along the melt/substrate interface shown in part (a) for composition (i.e., macro-segregation) and in part (b) solid fraction, both shown with variations in contact layer response. Dashed line indicates location of cooling water inlets. Results are for conditions $T_i = 988$ K, $U_b = 0.14$ m/s, $H = 10$ mm.

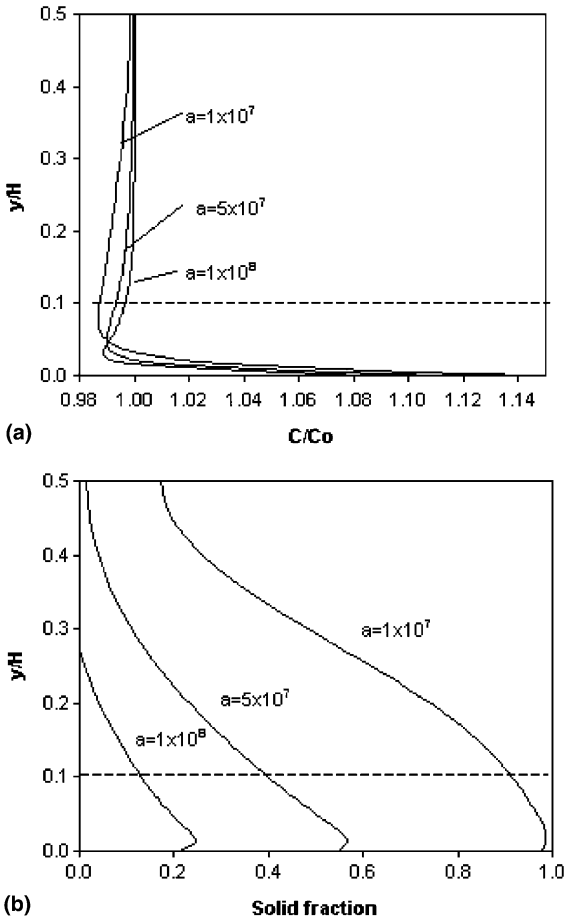

Fig. 8. Cast cross-section profiles at the exit of the contact zone ($x/L = 1$) shown in part (a) for composition (i.e., macro-segregation) and in part (b) solid fraction, both shown with variations in contact layer response. Dashed line indicates height of the nosepiece. Results are for conditions $T_i = 988$ K, $U_b = 0.14$ m/s, $H = 10$ mm.

fraction profiles shown for $a = 1 \times 10^8$ suggest that the macro-segregation will be further reduced at locations $x/L > 1$ since a significant solid fraction has not yet developed at the surface. It should be noted that in these calculations interdendritic fluid flow due to density variations are included but are small compared to the influence of forced convection on solute transport.

10. Conclusions

A CFD model has been developed for simulating the heat and mass transfer behavior of a liquid metal on a moving substrate. The model couples the important features of water cooling, substrate heat transfer (including motion), metal/substrate contact heat transfer and metal flow with solidification. The results compare well with strip casting of an Al–4.5 wt%Cu alloy in terms of the average heat flux removal in the initial contact zone, as well as centerline cooling rate. From the results, the contact layer model integrated into the CFD model highlights its important role in controlling excessive heat removal rates. A particular feature is that with solidification of the alloy delayed (with a highly active contact layer) any macro-segregation occurring as a result of non-equilibrium flow conditions near the initial metal contact can be diffused back into the melt, thus reducing the possibility of severe macro-segregation near the surface. This is not the case if the contact layer is only mildly active where a solid shell quickly forms and traps the composition variation into the surface. As the model at present assumes only the most basic features (at the microscale) of solid formation at the surface, i.e., dendritic columnar structures moving at the belt speed under local equilibrium, the results can only provide at best qualitative trends and require detailed experimental data on final cast structures to suggest further modeling of the initial surface conditions. This would involve considering effects of undercooling and various models for the solid morphology including when the solid would attach to the substrate. All of these features play a role in the macro-segregation predictions and ultimately predictions on final surface microstructure. However, this said, the model provides a basis for further development of microscale models since all of the key macroscale influences are present in the solution.

Acknowledgement

The authors would like to thank Alcan International Ltd. and the Natural Sciences and Engineering Research Council of Canada (NSERC) for support of this work through an NSERC Collaborative Research and Development Grant (CRDPJ-248034-01).

Appendix A. Temperature/solid fraction calculation

A.1. Temperature update

Following the solution of the governing transport equations an enthalpy and species distribution is available for the melt zone, which, along with the binary-phase diagram, can be used to determine the temperature distribution. In doing this local thermal equilibrium is assumed along with equilibrium species transport according to the Lever rule. In Fig. 9 is shown a linearized binary-phase diagram with phase boundaries shown relevant to solid–liquid phase transition. The enthalpy for the solidus and liquidus lines (h_s and h_l) and eutectic points (h_{se} and h_{le}) are defined as

$$\begin{aligned} h_s &= c_{ps} T_s \\ h_l &= c_{pl} T_l + (c_{ps} - c_{pl}) T_e + h_f \\ h_{se} &= c_{ps} T_e \\ h_{le} &= h_{se} + h_f \end{aligned} \tag{22}$$

where the specific heats of each phase, c_{ps} and c_{pl}, are assumed constant and the heat of fusion, h_f, is fixed at the eutectic temperature T_e. The solidus and liquidus temperatures are dependent on the composition through the equations:

$$\begin{aligned} T_l &= T_m + m_l c_l^\alpha \\ T_s &= T_m + m_s c_s^\alpha \end{aligned} \tag{23}$$

where m_l and m_s are the slopes of the solidus and liquidus lines in Fig. 9 and T_m the melting temperature for a pure substance. The solidus and liquidus compositions are related through the equilibrium partition coefficient given for the alloy where

$$k_p = \frac{m_l}{m_s} = \frac{c_s^\alpha}{c_l^\alpha} \tag{24}$$

With the liquidus, solidus and eutectic enthalpy boundaries defined then the mixture enthalpy, defined as shown in Eqs. (1) and (2), can be isolated at a known mixture composition c^α to determine temperature from the phase diagram. In this process there are two cases to consider as shown in Fig. 9 for a non-eutectic solidification path (1–2) or a path that results in eutectic composition (3–4).

The procedure follows the steps at a known c^α:

- If $h > h_l$ then the liquid metal temperature is

$$T = \frac{h - (c_{ps} - c_{pl}) T_e - h_f}{c_{pl}} \tag{25}$$

- If h_e (or h_s)$< h \leqslant h_l$ then a solution of the quadratic equation

$$0 = (n_1 + n_2) T^2 - (n_1 T_l + n_2 T_m + n_3 + n_4) T + n_5 \tag{26a}$$

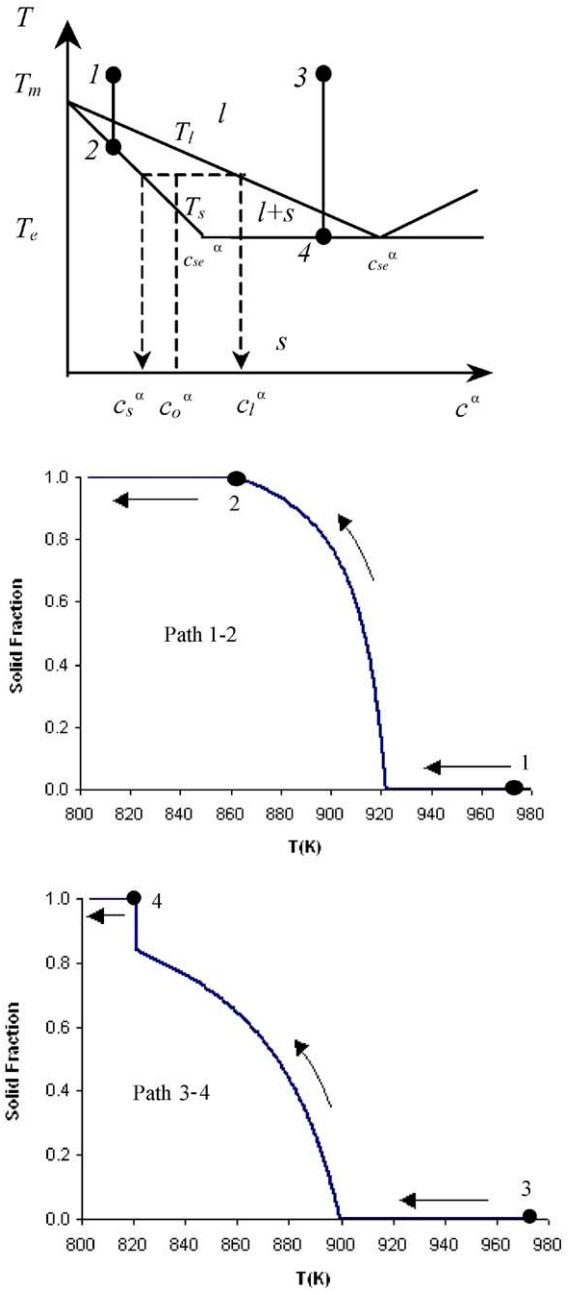

Fig. 9. Binary alloy (Al–Cu4.5 wt%) simplified phase diagram with non-eutectic (1–2) and eutectic (3–4) solidification paths shown.

where

$$\begin{aligned} n_1 &= c_{ps} - c_{pl} \\ n_2 &= c_{pl}(1-k_p) \\ n_3 &= (c_{ps} - c_{pl})T_e + h_f \\ n_4 &= (h - n_3)(1-k_p) \\ n_5 &= n_3 T_{liq} + n_4 T_m \end{aligned} \tag{26b}$$

provides the two-phase non-eutectic mixture temperature.

- If $c^\alpha < c^\alpha_{se}$ and $h \leqslant h_s$ then for the non-eutectic solid

$$T = \frac{h}{c_{ps}} \tag{27}$$

- If $c^\alpha_{se} \leqslant c^\alpha$ and $h_{se} < h \leqslant h_{le}$ then during eutectic phase change

$$T = T_e \tag{28}$$

- If $c^\alpha_{se} \leqslant c^\alpha$ and $h \leqslant h_{se}$ then for eutectic solid

$$T = \frac{h}{c_{ps}} \tag{29}$$

In Fig. 9 is shown the temperature history for cooling along a fixed composition where $c^\alpha < c^\alpha_{se}$ (path 1–2), or when $c^\alpha_{se} \leqslant c^\alpha$ (path 3–4), using the logic outlined above. In the first case the cooling is never isothermal however in the second case, depending on the eutectic composition, the cooling is isothermal through the eutectic point.

A.2. Solid fraction update

The solid fraction that is not eutectic can be evaluated from the known temperature field as follows:

$$f_s = \frac{c^\alpha_l - c^\alpha}{c^\alpha_l - c^\alpha_s} = \frac{T - T_l}{T - T_m} \cdot \frac{1}{1-k_p} \tag{30}$$

while in the eutectic case the solid fraction can be determined from the enthalpy distribution as follows:

$$f_s = \frac{h_e - h_{se}}{h_f} \tag{31}$$

Appendix B. Numerical model: contact layer

The contact layer involves a thin volume along the surface of the cooling substrate of which its thickness and gas volume fraction is not known. To resolve this Eqs. (16) and (18) must be solved in an iterative forward marching scheme to obtain the distribution of α_g and δ using the latest available temperature distribution for the contact layer. The solution of Eqs. (16) and (18) begins with a Newton–Raphson linearization of the non-linear terms at the *e*-face conditions (see Fig. 2). Beginning with *e*-face in Eq. (16):

$$\begin{aligned} (\rho_g U_b \alpha_g \delta)_e = {} & (\rho_g U_b \alpha_g \delta)^0_e + (\rho_g U_b \alpha_g)^0_e (\delta - \delta^0) \\ & + (\rho_g U_b \delta)^0_e (\alpha_g - \alpha^0_g) \end{aligned} \tag{32}$$

which reduces to

$$(\rho_g U_b \alpha_g \delta)_e = -(\rho_g U_b \alpha_g \delta)^0_e + (\rho_g U_b \alpha_g)^0_e \delta + (\rho_g U_b \delta)^0_e \alpha_g \tag{33}$$

and when substituted into the vapor conservation equation (Eq. (16)) we obtain

$$(\rho_g U_b \alpha_g)_e^0 \delta + (\rho_g U_b \delta)_e^0 \alpha_g = (S\bar{\delta}\Delta x)^0 + (\rho_g U_b \alpha_g \delta)_w + (\rho_g U_b \alpha_g \delta)_e^0 \quad (34)$$

A similar approach applied to the *e*-face conditions in Eq. (18) leads to a representation of the *e*-face conditions with

$$((\rho_{g-l}\alpha_g + \rho_l)U_b\delta)_e = -(\rho_{g-l}U_b\alpha_g\delta)_e^0 + ((\rho_{g-l}\alpha_g + \rho_l)U_b)_e^0\delta + (\rho_{g-l}U_b\delta)_e^0\alpha_g \quad (35)$$

and substitution into the mixture mass Eq. (18) we arrive at the final equation:

$$((\rho_{g-l}\alpha_g + \rho_l)U_b)_e^0\delta + (\rho_{g-l}U_b\delta)_e^0\alpha_g = ((\rho_{g-l}\alpha_g + \rho_l)U_b\delta)_w + (\rho_{g-l}U_b\alpha_g\delta)_e^0 \quad (36)$$

Eqs. (34) and (36) can be used in a forward marching scheme beginning from the leading edge of the substrate where the initial conditions of $\alpha_g = 0$ and $\delta = \delta^0$ are known at the *w*-face conditions for the first control-volume (see Fig. 2). Repetitive application of Eqs. (34) and (36), for a given control-volume, will converge to a final α_g and δ at the *e*-face. The *e* -face conditions are then used as the known *w*-face conditions for the next forward control-volume. This is repetitively applied along the length of the substrate.

References

[1] V.R. Voller, C. Prakash, A fixed-grid numerical modelling methodology for convection/diffusion mushy region phase change problems, Int. J. Heat Mass Transfer 30 (1987) 1709–1719.

[2] V.R. Voller, C.R. Swaminathan, B.G. Thomas, Fixed grid techniques for phase change problems: a review, Int. J. Num. Meth. Eng. 30 (1990) 875–898.

[3] C.J. Vreeman, M.J.M. Krane, F.P. Incropera, The effect of free-floating dendrites and convection on macrosegregation in direct chill cast aluminum alloys Part I: model development, Int. J. Heat Mass Transfer 43 (2000) 677–686.

[4] C.J. Vreeman, F.P. Incropera, The effect of free-floating dendrites and convection on macrosegregation in direct chill cast aluminum alloys. Part II: predictions for Al–Cu and Al–Mg alloys, Int. J. Heat Mass Transfer 43 (2000) 677–686.

[5] C. Tangthieng, F.B. Cheung, Thermosolutal transport and macrosegregation during freeze coating of a binary substance on a continuous moving object, Int. J. Heat Mass Transfer 46 (2003) 2313–2327.

[6] A.V. Kuznetsov, Parametric study of macrosegregation in the horizontal strip casting process for different cooling rates and different casting speeds, Heat Mass Transfer 35 (1999) 197–203.

[7] A.V. Kuznetsov, Investigation of the coupled heat transfer, fluid flow and solute transport during the strip casting process, Int. J. Heat Mass Transfer 40 (1997) 2949–2961.

[8] A.G. Gerber, C. Ng, M. Galerneault, Surface-oriented melt/substrate heat transfer model in aluminum strip casting, Metall. Trans. B 35 (2) (2004) 351–361.

[9] W.D. Bennon, F.P. Incropera, Numerical analysis of binary solid–liquid phase change using a continuum model, Numer. Heat Transfer 13 (1988) 266–296.

[10] J. Ni, F.P. Incropera, Extension of the continuum model for transport phenomena occurring during metal alloy solidification—I. The conservation equations, Int. J. Heat Mass Transfer 38 (7) (1995) 1271–1284.

[11] D.R. Poirier, Permeability for flow of interdendritic liquid in columnar-dendritic alloys, Metall. Trans. B 18 (1987) 245–255.

[12] H. Schlichting, Boundary-layer Theory, seventh ed., McGraw-Hill, New York, 1979.

[13] B.E. Launder, D.B. Spalding, The numerical computation of turbulent flows, Comput. Meth. Appl. Mech. Eng. 3 (1974) 269–289.

[14] G.E. Schneider, M.J. Raw, Control volume finite-element method for heat transfer and fluid flow using collocated variables—1. Computational procedure, Numer. Heat Transfer 11 (1987) 363–390.

[15] M. Raw, Robustness of coupled algebraic multigrid for the Navier–Stokes equations, AIAA paper 96-0297, 1996.

[16] Theory Documentation, CFX-TASCflow V2.12, AEA Technology ESL, June 2001.

[17] G.L. Leone, Y. D'Anjou, J. Sulzer, Alcan belt casting processProceedings of the Ingot and Continuous Casting Process Technology Seminar for Flat Rolled Products, vol. 2, The Aluminum Association, 1989, p. 581.

[18] S. Hamer, B. Taraglio, C. Romanowski, Light Metal Age, October 2002, pp. 6–17.

[19] M.C. Flemings, Solidification Processing, McGraw-Hill, New York, 1974.